Ground ice estimation in permafrost samples using industrial Computed Tomography

Mahya Roustaei [1,2*], Joel Pumple [1], Jordan Harvey [1], and Duane Froese [1,*]

5   [1] Department of Earth and Atmospheric Sciences, University of Alberta, Edmonton, Canada
     [2] Geotechnics Laboratory, Ghent University, Technologiepark 68, 9052 Zwijnaarde, Belgium

Correspondence to: Mahya Roustaei (Mahya.roustaei@ugent.be) or Duane Froese (duane.froese@ualberta.ca)

Abstract. The distribution and abundance of ground ice in permafrost is a fundamental property that determines the potential
for thaw subsidence and terrain effects of permafrost landscapes. However, most methods to characterize permafrost are

10 destructive and of low resolution. Here, some of the limitations of traditional destructive methods are overcome using
industrial computed tomography (CT) scanning to systematically log permafrost cores, visualize cryostructures, measure
frozen bulk density, and estimate volumetric and excess ice contents non-destructively. The results show strong agreement
with destructive analyses as well as recent developments using a multi-sensor core logger (MSCL), demonstrating that these
approaches can produce consistent results, and provide the added benefit of enhanced digital archives of permafrost physical

15 properties. Development of standardized and interoperable methods for permafrost characterization will build more robust
permafrost datasets and strengthen efforts to understand future thaw trajectories of permafrost landscapes.

1 Introduction

Permafrost is often characterized by the presence of excess ice, or ground ice that exceeds the total pore volume that the ground would have under unfrozen conditions (Brown et al., 1997; Zhang et al., 1999; Cai et al., 2020; Van Everdingen, 1998). The

20 presence of excess ice can affect the permafrost thermal regime, and landscape structure, and is proportional to thaw settlement following disturbance (Schramm and Becht, 2019). Widespread thawing of permafrost is expected under a warmer future climate, and modelling studies suggest large-scale degradation of near-surface permafrost by the end of this century (Lawrence et al., 2008, 2011; Cai et al., 2020). Past studies have illustrated that the presence of excess ice and its distribution in permafrost can significantly affect the rate of permafrost thaw and consequently Arctic ecosystems (Kokelj and Jorgenson, 2013;

25 Westermann et al., 2016; Nitzbon et al., 2020). Better estimation of ground ice is important for improving existing methods for mapping the distribution of excess ice at landscape scales and predicting the impacts of permafrost thaw (Cai et al. 2020).

Over the last several decades there have been rapid advances in the use of non-destructive methods for the investigation of internal textures and physical properties of frozen materials. One of these techniques is micro-computed tomography (µCT) which has been a useful tool in permafrost research since the initial studies by Calmels and Allard (2004,

30 2008). In those pioneering studies, the authors used µCT to measure ice and gas contents in ice-rich permafrost and established links between permafrost landforms and microscale cryostructures. Recent work has focused on cryostructures (Calmels et al., 2010; Fan et al., 2021), excess ice determination (Lapalme et al., 2017), distribution and consolidation of soil between ice lenses (Torrance et al., 2008), soil degradation in freeze-thaw cycles (Nguyen et al., 2019; Wang et al., 2018, 2017; Roustaei et al., 2022b; Roustaei et al., 2024), quantification of micro-lenticular ice lens formation (Darrow and Lieblappen, 2020),

35 unfrozen water content (Roustaei et al., 2022a), and composition and microstructural investigation of permafrost (Nitzbon et al., 2020). However, there are few studies that test the application of CT in quantifying both the excess ice content and volumetric ice content of frozen soils and comparing these data to established methods at similar spatial scales.

This study uses CT imaging as a non-destructive method to tackle the limitations of traditional ground ice classification methods by measuring frozen bulk density and estimating excess ice and volumetric ice contents quantitatively

40 from five permafrost samples at a high spatial resolution. The CT scanner used in this study is a cabinet-based industrial CT scanner commonly used in the automotive and manufacturing industries. The main difference between an industrial CT scanner and a medical CT scanner is the higher peak voltage, allowing greater potential penetration and greater image resolution. A new approach is also implemented for collecting CT scans with an internal standard (water) to calibrate the resulting linear attenuation coefficients into real density (g/cm^3). All CT density and volumetric ice content results are compared to a recent

45 study using the same cores but a different non-destructive method (Pumple et al., 2023), and the advantages of each are discussed. Finally, a quantitative comparison between the excess ice results collected via the destructive cuboid method and the CT image analysis is presented to show the reliability of the methods, including a sensitivity analysis to illustrate the effect of spatial resolution on excess ice estimations. The results of this study will help build more robust permafrost datasets and strengthen future efforts to map permafrost terrain and establish thaw sensitivity.

2 Methods and Materials

2.1 Materials

Five cores were compared in this study, each representing common materials encountered in permafrost regions and containing a relatively simple vertical cryostratigraphy ~~to minimize the impact of lateral heterogeneity~~ (Table 1). The Permafrost ArChives Science (PACS) Laboratory hosts a specialized imaging space where both the Nikon XTH 225 ST and the Geotek multi-sensor core logger (Pumple et al., 2024) are located. The imaging space is kept at 23 °C and as a result, special consideration had to be taken when working with frozen materials. We use an insulated sample container to keep samples frozen during the scanning process ~~which~~ is discussed further in section 2.5.

2.2 Sampling Process

The sampling process for this study needed consideration to ensure the destructive and non-destructive results were comparable. As such physical cores were run through all non-destructive data collection methods prior to subsampling. During subsampling, a duplicate transect of the cuboid samples was collected from the middle of the core to allow non-destructive data at a higher resolution on one set of the subsampled cubes. As seen in Figure 1, this resulted in the cuboids flanking either side of the MSCL and CT results which were collected from a central transect on the half-core.

2.3 Physical Density Measurements

Ground-ice content is typically expressed either as the *gravimetric moisture/ice content* (the ratio of the mass of the ice in a sample to the mass of the dry sample) or the *volumetric moisture/ice content* (the ratio of the volume of ice in a sample to the volume of the whole sample) (Van Everdingen, 1998). Similar to thaw-strain measurements in geotechnical investigations (Crory, 1973; Shur, 1988; Pullman et al., 2007; Kanevskiy et al., 2012), Kokelj and Burn (2003) and O'Neill and Burn (2012) ~~both~~ applied a method for destructively extracting excess ice content measurements from frozen samples. This method includes the complete thaw, homogenization, and settling time of the sample to extract the supernatant water content and estimate excess ice content. Their method does not require measurement of frozen sample volume since the volumes of sediment as well as the supernatant water should be recorded from the beakers containing the samples once completely thawed. The excess ice content (E_i) of the samples can then be estimated by the equation (Kokelj and Burn, 2003):

$$(Ei) = \frac{(Wv * 1.09)}{(Sv + Wv * 1.09)} * 100 \qquad (1)$$

Where Wv is the volume of supernatant water (cm^3), multiplied by 1.09 to estimate the equivalent volume of ice, and Sv is the volume of saturated sediment (cm^3).

This study takes an approach similar to Kokelj and Burn (2003) in that the supernatant water content is destructively assessed in order to calculate excess ice content. However, since the volume of soil samples was precisely measured in this study using the cuboid method, volumetric ice contents were also measured. Because in some soils, such as peat, excess ice

80   will be absorbed by the soil skeleton upon thaw (Johnston, 1981), the Kokelj and Burn method was adjusted for samples with high organic contents by applying a slight pressure on the thawed cube and extraction of the released water. Additionally, the organic content of each sample was measured via loss on ignition (LOI) (Heiri et al., 2001). The cuboid method, described by Bandara et al. (2019) and Pumple et al., (2024), is similar to other volumetric and gravimetric methods used to measure bulk density (particularly peat deposits) and ice content, but takes advantage of the ice-rich properties of frozen cores which allow

85   for a greater degree of sampling precision. Processing is undertaken in a walk-in freezer following methods outlined in Pumple et al. (2024).

2.4 Multi Sensor Core Logger (MSCL)

The PACS Laboratory MSCL is a floor-mounted, automated logging system, manufactured by Geotek, which can be used to analyse whole or split cores. This core logger is equipped with two magnetic susceptibility instruments, a line-scan camera,

90   and a Caesium-137 (^{137}Cs) gamma source and detector which provides measurements of gamma attenuation. Pumple et al. (2024) provides additional details on the methods used for the MSCL data collection and calibration. The combination of the frozen bulk density results from the gamma attenuation, an estimation of soil density, and the equation presented for volumetric ice content, following Lin et al. (2020), can be used to estimate bulk ice content non-destructively using the MSCL (Pumple et al., 2024).

95   **2.5 Industrial Micro Computerized Tomography**

Micro Computed tomography (μCT) was used to examine the ice, sediment, and gas contents of several permafrost cores and cube samples. This method is a non-destructive technique that has been useful in the investigation of geological porous media (Ashi, 1997; Ketcham and Carlson, 2001; Kozaki et al., 2001; Flisch and Becker, 2007; Calmels and Allard, 2004; Van Geet et al., 2005; Tanaka et al., 2010; Nitzbon et al., 2020). It consists firstly in recording a set of two-dimensional X-ray radiographs

100   at multiple angles, and secondly reconstructing the 2D projections to form a 3D image using a mathematical algorithm. The final measurement unit presented in the histogram is the linear attenuation coefficient which depends on both the density and the electron density of the material (Ketcham and Carlson, 2001). This varies slightly from earlier permafrost CT studies that report values in Hounsfield units that are common in medical CT studies (eg. Calmels et al., 2010). In this study, internal calibration with a reference water sample at the time of scanning is used to convert the primary linear attenuation values

105   derived from the CT data directly to density (g/cm³).

The scans presented here were captured using a helical scan with a Nikon XTH 225 ST cabinet-based industrial computed tomography micro-CT scanner. The system uses an electronically adjustable 225 Kv 225W power source (Figure 2). This system includes both a tungsten rotating reflection target source and a tungsten fixed reflection target source coupled with a 16-bit 2000x2000 pixel detector capable of a focal spot size range of 3-121 μm depending on the size of the area of

110   interest and size of the object being scanned. The 10cm diameter frozen permafrost half cores were scanned with the reflection target source at 200 Kv 35 μa with an exposure time of 125 ms and a voxel (3D volume element representing pixel resolution

and slice thickness) size of 65 μm. The subsampled cubes from the cores were subsequently scanned with the rotating reflection target source at 225 Kv 133 μa with an exposure time of 125 ms and a voxel size of 25 μm. The images were reconstructed into three-dimensional grey-scale volumes using the Nikon CT pro 3D software and analyzed using ORS Dragonfly 2022 image processing software (ORS 2021).

This project was completed during development of an insulated sample holder for use in the CT scanner. Both cubes and cores were housed in the same style of a styrofoam container, however, the internal setup varied due to the size of the sample under investigation. Cores were placed in a larger styrofoam container with an inner diameter of 12 cm in the vertical position and an ice pack was placed directly above them (Figure 2B and C). For this experiment, all ice packs were cooled to -80 C prior to being added to the container at the start of the scan. The ice packs held the core's surface temperature below freezing for the duration of the scan. The cubes were held in a slightly smaller container with an inner diameter of 9 cm in a small plastic vial with a foam divider directly above (Figure 2D). The cubes were cooled with a small amount of dry ice placed on a perforated foam divider to bathe the underlying sample with cold air during scanning.

It should also be noted that the partial results for most full cores are due to a height restriction encountered during the helical scans. This restriction was resolved after cores were subsampled for the cuboid method. This means for some of the cores we were unable to compare the complete vertical data sets of the MSCL, cuboid, and CT results.

2.6 CT Calibration

The linear attenuation coefficient (μ) represents the energy attenuated within a single voxel volume while the voxel population is the population of voxels within a scan volume (Ketcham & Carlson, 2001). By creating a histogram (linear attenuation coefficient vs voxel population)with these values , distributions of relative grey values can be presented. If uncalibrated, the resulting grey values observed in the histogram of a CT scan appear as linear attenuation coefficients. The medical field has developed methods for converting linear attenuation coefficients to Hounsfield units and as a result, the Hounsfield scale has become commonly used in CT research (Hounsfield, 1973; Wellington and Vinegar, 1987; Duliu, 1999; Knoll, 2000; Ketcham and Carlson, 2001; Duchesne et al., 2009). Lee et al., 2015 took it one step further and converted mean Hounsfield unit values to bone mineral density values (mg/cm^3) via a linear regression analysis. A similar approach was used in this study by collecting the CT scans with an internal standard of known density (water) later used to calibrate the resulting linear attenuation coefficients into g/cm^3 using the Nikon CT Pro 3D software. It should be noted that all cores were scanned with ice, water, and aluminum calibration pieces of which water proved to be in closest agreement with destructive analyses. The aluminum calibration piece generally underestimated the bulk density while the ice calibration piece resulted in a slight overestimation. Overall, the water calibration produced the most accurate results apart from ice-poor sediments. The Nikon CT Pro 3D software uses a linear two-point calibration with the first fixed point being air (equal to zero) and the second a user-defined value based on a user-selected pixel population. A representative (local) population of pixels was selected from our water sample in a 2D slice of the scan and informed the expected average target value (1 g/cm^3). This results in the histogram displaying grey values in g/cm^3.

2.7 Image Processing

145

This study uses Dragonfly software (ORS 2021) to process the three-dimensional reconstructed X-ray tomographs of the frozen materials to segment, quantify, calculate, and illustrate the materials' physical properties. One of the main Dragonfly software features utilized in this study is the Otsu image thresholding method. The algorithm of this method, proposed by Nobuyuki Otsu (1979), performs automatic clustering-based image thresholding. In this method, it is assumed that there are two classes of pixels which are *foreground* and *background* pixels of the image. The optimum thresholding is calculated by distinguishing the two classes so that the minimum class variance is obtained (Kumar and Tiwari, 2019). This method was applied to the selected regions of interest to differentiate sediment and ice. This allows us to isolate the materials within our scans based on density and slowly slice away the lighter density portion (ice) until we are certain we have collected the target material range (often a mixture of ice and sediment). Figure 3 shows the ice (less dense material) being segmented from the surrounding sediment through multiple image processing steps using the Otsu method where only the background (less dense) portion of the previous step is added to the final result. This approach shows that applying the first image processing step will mainly extract the visible ice while using multiple Otsu analyses on the resulting image adds additional lower-density ice-rich mixtures (mainly pore ice) are extracted, e.g., the area shown inside the red circle of Figure 3B-D.

150

155

2.8 Region of Interest (ROI)

160

A series of ROIs were created in the half core CT results down the central vertical axis of the cores to mimic the data collection points of the MSCL as presented in Pumple et al., 2024. Figure 1 displays the ~~relative~~ location of these ROIs which were sized to match the spot size of the gamma-ray at the surface of the core, ~10 mm in diameter. The central point of each ROI was placed 5 mm apart resulting in a significant overlap between adjacent data points, again similar to the data collection process for the MSCL. In this study, all cores were calibrated so the histogram values were displayed in g/cm^3. To extract the frozen bulk density from each ROI, the mean grey values were extracted in calibrated density values (g/cm^3).

165

3 Results and Discussions

3.1 Image Segmentation

In CT the ability to differentiate materials depends on their respective linear attenuation coefficients, meaning materials with divergent densities and/or atomic numbers ~~are easier to differentiate~~ (Kyle and Ketcham, 2015). Analysing a multi-modal histogram of a CT image is straightforward for material differentiation while materials with ~~closed~~ densities appear as a single peak in the histogram. In addition to the relative density of the scanned materials, the image resolution or voxel size also directly impacts the image segmentation process. The voxel size can impact the image segmentation through the partial volume effect which relates directly to the finite spatial resolution of the scan and for geological samples, the grain size distribution (Soret et al., 2007; Nitzbon et al., 2022).

170

175   Figures 4 A and B show one slice of a small ROI and its histogram from 5 different cores of this study. The differences in the shapes of the histograms are due to the different sediment densities ~~of the sample~~. The diamicton core has the highest sediment density and a bimodal histogram in which the first mode represents ice and the second is related to the sediments and clasts. Whereas in the other cores, ice and sediment appear as a single mode. Image segmentation of these slices using the Otsu method resulted in the differentiation of 5 different materials on the basis of their relative densities; air, low ice, high ice, low

180   sediment, and high sediment shown in Figures 4 B and C. Low ice comprises primarily visual or excess ice while high ice mainly results from extraction of pore ice or ice proximal to sediment (sediment-rich ice). It should be noted that the high ice appears denser due to the partial volume effect caused by proximal higher density sediments. Low sediment and high sediment are also differentiating ice-rich sediments and sediments with lower and higher densities, respectively. Figure 5 illustrates the image segmentation results in the whole diamicton core. These figures illustrate the effectiveness of the Otsu method in

185   generating consistent segmentation results and offers an alternative to the visual inspection method that depends strongly on the inspector's visual acuity and experience.

3.2 Core Results

190   ~~The results presented below combine the image processing analysis of CT images from 5 cores and a systematic quantitative comparison between the Cuboid (destructive method) and the recent non-destructive method (Pumple et al., 2024).~~ Physical properties of the permafrost samples, determined from the cuboids, including frozen bulk density, volumetric (VIC) and excess ice contents (EIC), and organic contents are plotted versus the depth of the cores and shown as B, C, and D in Figures 6-10, respectively. The vertical cross-section photo of the core (A) is also presented in these figures. The non-destructive CT results

195   for VIC, EIC, and frozen bulk density for each core are then compared to both the destructive cuboid and non-destructive MSCL results using an average root mean square error (RMSE) (Table 2).

3.2.1 Ice-rich Silt Core (BH18-211):

Figure 6 shows the destructive (cuboid) and non-destructive (CT and MSCL) results of the ice-rich silt core, illustrating that the CT frozen bulk densities are in strong agreement with both the cuboid (RMSE = 0.12 g/cm^3) and MSCL (RMSE = 0.14

200   g/cm^3) results. This core has a high organic content (8-19% organic carbon), micro-lenticular and layered cryostructures, and 66% silt. Cuboid physical EIC and VIC measurements range from 19-34% and 68-76%, respectively, while the CT EIC and VIC estimates range from 20-68% and 32-74% at the same depths where cuboid measurements were collected. The 65 μm EIC (redline in Figure 6C) shows good agreement with the cuboid EICs (RMSE = 9%) apart from the ice layer where the cuboid's relatively low sample resolution results in an averaging of the ice content across the ice layer. ~~The MSCL results~~

205   ~~consistently display lower values relative to the cuboid data.~~ The 65 μm VICs (black line in Figure 6C) illustrate the resolution limitation in extracting the pore ice of this sandy silt core while the 25 μm VICs shown as black cubes in the same plot tackle

this limitation and agree well with VICs extracted from the Cuboid method (RMSE = 7%). The MSCL VICs follow the same trend as the cuboid data (Fig 6-C) but consistently trend toward lower values in the ice-poor regions.

3.2.2 Transition Core (BH12F-138):

210 Figure 7 shows the results of the transition core from both destructive (cuboid) and non-destructive (CT and MSCL) methods, illustrating a sharp boundary between an ice-rich silty peat, containing massive and rare crustal cryostructures, and an ice-poor inorganic silt with a mainly micro-lenticular cryostructure. The organic content of the core's top section, ranging from 53-71%, highlights this transition (Figure 7D). Cuboid physical EIC and VIC measurements range from 6-28% and 64-88%, respectively, while the CT EIC and VIC estimates range from 9-33% and 42-95% at the same depths where cuboid

215 measurements were collected. This figure also shows that the CT bulk density results are in strong agreement with both the cuboid (RMSE = 0.13 g/cm³) and gamma attenuation data (RMSE = 0.06 g/cm³) (Pumple et al., 2024). The 65 µm EIC results (red line in Figure 7-C) follow the cuboid results (RMSE = 5%) in the silty section. The 65 µm VIC (black line in Figure 7C) resolves more than 50% of pore ice, while the higher resolution (25 µm, black cubes in Figure 7C), estimates up to 100% (RMSE = 3%).

3.2.3 Diamicton Core (BS19-3-6):

Figure 8 illustrates the destructive (cuboid) and non-destructive (CT and MSCL) results of the diamicton core. This ice-rich diamicton contains both suspended and crustal cryostructures and more than 50% silt (Table 1). Overall, the bulk density and ice measurements from CT display high concordance with the gamma attenuation (RMSE = 0.14 g/cm³), and cuboid (RMSE = 0.14 g/cm³) methods (Figure 8). Cuboid physical EIC and VIC measurements range from 30-50% and 48-66%, respectively,

225 while the CT EIC and VIC estimates range from 22-57% and 36-77% at the same depths as the cuboid measurements. The 65 µm EIC results (red line in Figure 7C) follow the cuboid results (RMSE = 8%). The only point where the datasets differ notably is at 2-4 cm depth where the MSCL dataset shifts towards lower density values due to the core's lateral heterogeneity while the CT density still lines up well with the cuboid result. The ice contents of this cube are also lower than CT and MSCL results. This is due to the collection procedure of the cubes which were off-center to accommodate a duplicate run of cubes down the

230 middle of the core for CT imaging and destructive measurements (as shown in Figure 1). This single cube highlights the importance of considering the difference in the locations of ROIs between CT/MSCL and the cuboid methods. Moreover, at this depth in the core cuboid sample, there was a clast which resulted in a local density high and lower ice content.

In this core, the 65 µm VICs agree well with the cuboid-VICs, MSCL (RMSE = 4%) ice contents, and 25 µm cube scan results (RMSE = 3%) while in the transition core, the 65 µm VICs underestimated the other VIC results. The difference

235 between the 65 um VIC results and other VIC results for all cores except the diamict could be a result of the sample's grain size as the diamict has high clay content (~18%) relative to the other cores (~8-12%) (Table 1).

3.2.4 Ice-poor Silt Core (BH20B-337):

Figure 9 shows the results of the ice-poor silt core from both destructive (cuboid) and non-destructive (CT and MSCL) methods, illustrating a massive (non-visible) cryostructure within this inorganic silt that highlights the relatively low overall

240 ice content throughout the core. This core has little variability throughout its profile. The CT bulk densities are consistent with both the cuboid (RMSE = 0.14 g/cm^3) and gamma attenuation data (RMSE = 0.14 g/cm^3) (Figure 9). The 65 μm EIC results compare well with the cuboid EIC results (RMSE = 5%) while the 25 μm cube scan ice contents show strong agreement (RMSE = 3%) with the volumetric cuboid ice content estimates.

3.2.5 Peat Core (DH13-589):

245 Figure 10 illustrates the destructive (cuboid) and non-destructive (CT and MSCL) characterization results of the peat core, with little variability throughout its profile. The core is formed of homogenous organics, with an organic-matrix cryostructure of visible ice within the densely packed peat. The CT bulk density results are similar to both the cuboid (RMSE = 0.05 g/cm^3) and gamma attenuation results (RMSE = 0.03 g/cm^3) (Figure 10). The 65 μm ice content results (39-48% of EIC) are also in accordance with the cuboid excess ice results (RMSE = 4%). The 65 μm and 25 μm VICs are both showing good estimates of

250 VICs (RMSE = 1%). It should be noted that the adjusted method for extraction of supernatant water, using slight pressure to release water from organic matrix, was applied to the cubes of this core.

3.3 Sensitivity analysis

In this study we investigate the impact of resolution on the delineation between ice and sediment, using repeat scans on the same cube. Initially, the half cores (10 cm diameter) were scanned with a 65 μm voxel size. This was due to the physical size

255 (width) of the imaging window. The smaller size of the cubes, however, presented an opportunity to collect data from the same material but at a resolution of 25 μm. Some of the cubes were also scanned at the same 65 μm resolution as the half cores to make a direct comparison. Figure 11 shows the same slice location and orientation from the same cube at two different resolutions.

An ROI, shown as a red square in Figure 11, was then selected in each cube scan to make a direct comparison between

260 the delineated (Otsu split) ice contents from image processing and the ice contents determined from the cuboid results. As reference points, the cuboid ice content results for this cube were as follows: 22% EIC and 65% VIC. Figure 12 shows the collected data from repeat image processing steps using the Otsu method of each cube as well as the cuboid results. The initial image processing steps for both the 25 μm and 65 μm scans closely capture the expected value of the EIC. However, only the 25 μm cube captures a representative value relative to the cuboid data for the expected VIC. This value is reached after 6 image

265 processing steps using the Otsu method. The nature of the curve suggests that VIC cannot be delineated from the 65 μm resolution scans however EIC is possible. Given the sediment type present in the cubes is mostly sandy silt, the expected pore space would be in the range of 50 μm in size which is likely the difference between the results of these two scans. Additionally,

there is an observable increase in the amount of pore space or gas captured in the 25 μm resolution relative to the 65 μm. This difference highlights the 25 μm scan's increased potential to capture, and as a result segment, the different components within the scanned material.

3.4 Comparison of CT and Cuboid Density and Excess Ice Results:

Segmentation of the CT images using the Otsu method allows comparison of CT-derived bulk densities, excess ice, and volumetric ice contents with estimates from the cuboid method at similar resolution. We completed these comparisons at 65 μm and 25 μm (Figures 13, 14 and 15). These figures display good agreement for density, excess ice, and volumetric ice measurements with RMSE of 0.12 g/cm^3, 6%, and 3%, respectively. Additionally, the CT results compare well with the MSCL results for both density and VIC with RMSE's of 0.08 g/cm^3 and 7%, respectively (Figures 16 and 17). The differences between the estimated EICs from CT image processing (65 μm-whole core) and the measured ones from the cuboid method are due to the differing resolutions, i.e., 0.5 cm for CT and 2 cm for the cuboid method, as well as the slightly different locations of the regions of interest (previously described in section 2.2). The strong accordance of the VICs highlights the opportunity for higher resolution scans to estimate pore ice.

3.5 Comparison of Non-destructive Methods:

The results of this study show strong agreement between two non-destructive methods: CT and MSCL, and highlight the importance of continued development and refinement of non-destructive methods for extracting physical properties from permafrost materials.

The CT method we present allows for whole core high-resolution (65 μm) three-dimensional imaging of cores, measurement of bulk density and estimation of excess ice contents at a user-defined scale. This contrasts with MSCL which is restricted to a fixed data collection transect down the center of the core (~ 1cm wide) with a maximum sample resolution of ~ 0.5 cm, high resolution (25 μm) 2-dimensional half-core images and currently provides only volumetric ice estimates, and no direct estimates of excess ice. The CT method can estimate volumetric ice contents but requires cores to be subsampled to a smaller size to allow for finer resolution scans (25 um).

It is worth noting that the MSCL provides a more rapid method for collecting bulk density and volumetric ice content estimations relative to the CT method. However, in addition to bulk density and volumetric ice content estimations, the CT method can provide direct estimates of excess ice content. Therefore, in terms of a non-destructive method for identifying and quantifying excess ice within permafrost cores the CT method provides a more robust approach although the image processing and acquisition costs are significantly greater.

4 Conclusions

This study investigated the application of high-resolution industrial CT scanning as a non-destructive method to tackle the limitations of traditional destructive methods, systematically log permafrost cores, visualize cryostructures, measure bulk density, and estimate volumetric and excess ice contents. Five permafrost cores, representing common materials encountered in permafrost regions, were scanned ~~at spatial resolut~~ ons of 65 and 25 μm. A new calibration method was used to extract real densities in g/cm³ directly from CT images. The initial identification of different materials from CT images showed 3 classes; air (gas), ice, and sediments while image processing of the scans using an automatic segmentation technique (Otsu method) illustrated significant density differences in ice and sediment classes. Image segmentation results using multiple image processing steps showed visual/excess ice as a lower density relative to the pore ice and delineated two sediment classes based on densities.

Since manual and visual thresholding is subject to operator experience and judgment and also not applicable in images with unimodal histograms related to materials with close densities (organic materials and ice), an automatic thresholding technique was used in this study to generate more consistent results.

Comparison of the image processing results and extracted physical properties of 5 permafrost cores were validated against a destructive method (cuboid) and the MSCL non-destructive method. The results showed strong agreement between these three methods (CT and cuboid) considering their differing resolutions and regions of interest with overall average RMSE's of 3%, 6% and 0.12 g/cm³ for VIC, EIC and density, respectively. This agreement demonstrates the applicability and reliability of non-destructive methods in tracking physical and cryostructural details of permafrost cores and producing replicable, cost-effective measurements.

A sensitivity analysis of the impact of differing resolutions on the delineation between ice and sediment showed that higher resolution scans generate more accurate VICs while the lower resolution scans are still sufficient for estimation of EICs and a rough estimation of VICs.

The proposed approach of this study will help build more robust permafrost datasets and strengthen future permafrost research efforts in mapping the distribution of excess ice and predicting thaw settlement. It also presents an opportunity to develop methods to extract more information from existing datasets based on an acute understanding of the relations between key physical permafrost properties. The next steps can be followed by using machine-learning-based image segmentation methods to generate datasets and explore the relations between physical permafrost properties.

Author contribution

MR, JP, DF, and JH planned the project; MR, JH, and JP developed the methods; MR, JH, and JP performed the measurements; MR and JH analyzed the data; MR, JP and JH wrote the manuscript draft; MR, JP, JH, and DF reviewed and edited the manuscript.

Competing interests

The authors declare that they have no conflict of interest.

Acknowledgements

330 The authors would like to thank Evan Francis who helped with sample preparation in earlier experiments. We would also like to thank Nikon Metrology for the support and constructive feedback they provided throughout the project. Casey Buchanan is thanked for collecting the diamict sample used in this study.

Financial support

This research was supported by the NSERC funded Permafrost Partnership Network for Canada (PermafrostNet) and NSERC
335 Discovery grant to Duane Froese. Laboratory infrastructure for the Permafrost Archives Laboratory was funded by Canadian Foundation for Innovation, Government of Alberta, and University of Alberta.

References

Ashi, J., Computed tomography scan image analysis of sediments, in Proc. ODP, Sci. Results, edited by Shipley, T. H., Y. Ogawa, P. Blum, and J. M. Bahr, 156, 151–159, 1997. Bandara, S., Froese, D. G., St. Louis, V. L., Cooke, C. A., and Calmels,
340 F.: Postdepositional Mercury Mobility in a Permafrost Peatland from Central Yukon, Canada, ACS Earth Sp. Chem., 3, 770–778, https://doi.org/10.1021/acsearthspacechem.9b00010, 2019.

Brown, J., Ferrians, O., Heginbottom, J., and Melnikov, E. S.: Circum-Arctic map of permafrost and ground-ice conditions, https://doi.org/10.3133/cp45, 1997.

Cai, L., Lee, H., Schanke Aas, K., and Westermann, S.: Projecting circum-Arctic excess-ground-ice melt with a sub-grid
345 representation in the Community Land Model, Cryosphere, 14, 4611–4626, https://doi.org/10.5194/tc-14-4611-2020, 2020.

Calmels, F. and Allard, M.: Ice segregation and gas distribution in permafrost using tomodensitometric analysis, Permafr. Periglac. Process., 15, 367–378, https://doi.org/10.1002/ppp.508, 2004.

Calmels, F. and Allard, M.: Segregated ice structures in various heaved permafrost landforms through CT Scan, Earth Surf. Process. Landforms, 33, 209–225, https://doi.org/10.1002/esp.1538, 2008.

350 Calmels, F., Clavano, W. R., and Froese, D. G.: Progress on X-ray computed tomography (CT) scanning in permfrost studies, in: GeoCalgary 2010 : the 63. Canadian geotechnical conference and 6. Canadian permafrost conference, Calgary, AB (Canada), 12-15 Sep , 1353–1358, 2010.

Crory, F.: Settlement associated with the thawing of permafrost, Hanover, New Hampshire, 599–607 pp., 1973.

Darrow, M. M. and Lieblappen, R. M.: Visualizing cation treatment effects on frozen clay soils through μCT scanning, Cold
355   Reg. Sci. Technol., 175, https://doi.org/10.1016/j.coldregions.2020.103085, 2020.

Duchesne, M. J., Moore, F., Long, B. F., , Labrie, J.: A rapid method for converting medical Computed Tomography scanner
topogram attenuation scale to Hounsfield Unit scale and to obtain relative density values. Engineering Geology 103, 100–105,
2009.

Duliu, O.: Computer axial tomography in geosciences: an overview. Earth-Sci. Rev.
360   48 (4), 265–281, 1999. https://doi.org/10.1016/S0012-8252(99)00056-2

Van Everdingen, R. O.: MULTI-LANGUAGE GLOSSARY of PERMAFROST and RELATED GROUND-ICE TERMS,
Calgary, 1998.

Fan, X., Lin, Z., Gao, Z., Meng, X., Niu, F., Luo, J., Yin, G., Zhou, F., Lan, A.: Cryostructures and ground ice content in ice-
rich permafrost area of the Qinghai-Tibet Plateau with Computed Tomography Scanning. Journal of Mountain Science. 18.
365   1208-1221. 10.1007/s11629-020-6197-x, 2021.

Flisch, A., and Becker, A.: Industrial X-ray computed tomography studies of lake sediment drill cores. In: Mees, F., Swennen,
R., Van Geet, M., Jacobs, P. (Eds.), Applications of X-ray Computed Tomography. Geological Society, London, Special
Publication, 215, pp. 205–212, 2003. https://doi.org/10.1144/GSL.SP.2003.215.01.19

Heiri, O., Lotter, A.F. and Lemcke, G., 2001. Loss on ignition as a method for estimating organic and carbonate content in
370   sediments: reproducibility   and   comparability   of   results.   Journal   of   paleolimnology,   25(1),   pp.101-110.
https://doi.org/10.1023/A:1008119611481.

Hounsfield, G.N.: Computerized transverse axial scanning (tomography). Part I. Description of system. Br. J. Radiol. 46 (552),
1016–1022, 1973. https://doi.org/10.1259/0007-1285-46-552-1016

Johnston, G. H.: Permafrost: engineering design and construction, National Research Council Canada. Associate Committee
375   on Geotechnical Research, 1981.

Jorgenson, M. T., Macander, M., Jorgenson, J. C., Ping, C. L., and Harden, J.: Ground ice and carbon characteristics of eroding
coastal permafrost at Beaufort Lagoon, northern Alaska, 495–500, 2003.

Kanevskiy, M., Shur, Y. L., Connor, B., and Dillon, M. R.: Study of the Ice-Rich Syngenetic Permafrost for Road Design
(Interior Alaska), in: Tenth International Conference on Permafrost TICOP, 191–196, 2012.

380   Ketcham, R. A. and Carlson, W. D.: Acquisition, optimization and interpretation of X-ray computed tomographic imagery:
applications to the geosciences, Comput. Geosci., 27, 381–400, https://doi.org/10.1016/S0098-3004(00)00116-3, 2001.

Kokelj, S. V. and Burn, C. R.: Ground ice and soluble cations in near-surface permafrost, Inuvik, Northwest Territories,
Canada, Permafr. Periglac. Process., 14, 275–289, https://doi.org/10.1002/ppp.458, 2003.

Kokelj, S. V. and Jorgenson, M. T.: Advances in Thermokarst Research, Permafr. Periglac. Process., 24, 108–119,
385   https://doi.org/10.1002/ppp.1779, 2013.

Kozaki, T., Suzuki, S., Kozai, N., Sato, S., and Ohashi, H.: Observation of Microstructures of Compacted Bentonite by Microfocus X-Ray Computerized Tomography (Micro-CT), J. Nucl. Sci. Technol., 38, 697–699, https://doi.org/10.1080/18811248.2001.9715085, 2001.

Knoll, G.F.: Radiation Detection and Measurement. John Wiley and Sons, New York, 1999.

390 Kumar and Tiwari: A Comparative Study of Otsu Thresholding and K-means Algorithm of Image Segmentation, Int. J. Eng. Tech. Res. , 9, 2019.

Kyle, J. R. and Ketcham, R. A.: Application of high resolution X-ray computed tomography to mineral deposit origin, evaluation, and processing, Ore Geol. Rev., 65, 821–839, https://doi.org/10.1016/j.oregeorev.2014.09.034, 2015.

Lapalme, C. M., Lacelle, D., Pollard, W., Fortier, D., Davila, A., and McKay, C. P.: Cryostratigraphy and the Sublimation

395 Unconformity in Permafrost from an Ultraxerous Environment, University Valley, McMurdo Dry Valleys of Antarctica, Permafr. Periglac. Process., 28, 649–662, https://doi.org/10.1002/ppp.1948, 2017.

Lawrence, D. M., Slater, A. G., Romanovsky, V. E., and Nicolsky, D. J.: Sensitivity of a model projection of near-surface permafrost degradation to soil column depth and representation of soil organic matter, J. Geophys. Res., 113, F02011, https://doi.org/10.1029/2007JF000883, 2008.

400 Nguyen, T. T. H., Cui, Y.-J., Ferber, V., Herrier, G., Ozturk, T., Plier, F., Puiatti, D., Salager, S., and Tang, A. M.: Effect of freeze-thaw cycles on mechanical strength of lime-treated fine-grained soils, Transp. Geotech., 21, 100281, https://doi.org/10.1016/j.trgeo.2019.100281, 2019.

Nitzbon, J., Westermann, S., Langer, M., Martin, L. C. P., Strauss, J., Laboor, S., and Boike, J.: Fast response of cold ice-rich permafrost in northeast Siberia to a warming climate, Nat. Commun., 11, 2201, https://doi.org/10.1038/s41467-020-15725-8,

405 2020.

O'Neill, H. B. and Burn, C. R.: Physical and temporal factors controlling the development of near-surface ground ice at Illisarvik, Western Arctic coast, Canada, Can. J. Earth Sci., 49, 1096–1110, https://doi.org/10.1139/E2012-043, 2012.

Object Research Systems. Dragonfly; Object Research Systems: Montreal, QC, Canada, 2021.

Otsu, N.: A Threshold Selection Method from Gray-Level Histograms, IEEE Trans. Syst. Man. Cybern., 9, 62–66,

410 https://doi.org/10.1109/TSMC.1979.4310076, 1979.

Pumple, J., Monteath, A., Harvey, J., Roustaei, M., Alvarez, A., Buchanan, C., & Froese, D. (2023). Non-destructive multi-sensor core logging allows rapid imaging, measurement of bulk density and estimation of ice content in permafrost cores. *EGUsphere*, *2023*, 1–27. https://doi.org/10.5194/egusphere-2023-571

Pullman, E. R., Jorgenson, M. T., and Shur, Y.: Thaw settlement in soils of the Arctic Coastal Plain, Alaska, Arctic, Antarct.

415 Alp. Res., 39, 468–476, https://doi.org/10.1657/1523-0430(05-045)[PULLMAN]2.0.CO;2, 2007.

Roustaei, M., Pumple, J., Harvey, J., and Froese, D.: Estimating ice and unfrozen water in permafrost samples using industrial computed tomography scanning, in: GeoCalgary 2022, 2022a.

Roustaei, M., Pumple, J., Hendry, M. T., Palat, A., and Froese, D.: Freeze-thaw impacts on macropore structure of fiber-reinforced clay by industrial computed tomography scanning, in: GeoCalgary 2022, 2022b.

420   Roustaei, M., Pumple, J., Hendry, M. T., Palat, A., and Froese, D.: Effect of freeze-thaw cycles on the macrostructure and failure mechanisms of fiber-reinforced clay using industrial computed tomography, in: Canadian Geotechnical Journal, 2024, https://doi.org/10.1139/cgj-2023-0136.

Schramm, L. A. and Becht, M.: Estimating excess ground ice in Arctic tundra landscapes by a statistical analysis of drained thermokarst lake basins-A comparison between research sites in Alaska, Institute of Geography, Catholic University of

425   Eichstätt - Ingolstadt, 2019.

Shur, Y. L.: The upper horizon of permafrost soils, in: Proceedings of the Fifth International Conference on Permafrost, 867–871, 1988.

Soret M, Bacharach SL, Buvat I. Partial-volume effect in PET tumor imaging. J Nucl Med. 48:932–945, 2007.

Tanaka, E. Y., Yoo, J. H., Rodrigues, A. J., Utiyama, E. M., Birolini, D., and Rasslan, S.: A computerized tomography scan

430   method for calculating the hernia sac and abdominal cavity volume in complex large incisional hernia with loss of domain, Hernia, 14, 63–69, https://doi.org/10.1007/s10029-009-0560-8, 2010.

Torrance, J. K., Elliot, T., Martin, R., and Heck, R. J.: X-ray computed tomography of frozen soil, Cold Reg. Sci. Technol., 53, 75–82, https://doi.org/10.1016/j.coldregions.2007.04.010, 2008.

Wang, S., Yang, P., and Yang, Z. (Joey): Characterization of freeze–thaw effects within clay by 3D X-ray Computed

435   Tomography, Cold Reg. Sci. Technol., 148, 13–21, https://doi.org/10.1016/j.coldregions.2018.01.001, 2018.

Wellington, S.L., Vinegar, H.J.: X-ray computerized tomography. J. Pet. Technol. 39 (8), 885–898,1987.

Westermann, S., Langer, M., Boike, J., Heikenfeld, M., Peter, M., Etzelmüller, B., and Krinner, G.: Simulating the thermal regime and thaw processes of ice-rich permafrost ground with the land-surface model CryoGrid 3, Geosci. Model Dev., 9, 523–546, https://doi.org/10.5194/gmd-9-523-2016, 2016.

440   Zhang, T., Barry, R. G., Knowles, K., Heginbottom, J. A., and Brown, J.: Statistics and characteristics of permafrost and ground-ice distribution in the Northern Hemisphere 1, Polar Geogr., 23, 132–154, https://doi.org/10.1080/10889379909377670, 1999.

445

450

455

Table 1: Sampling location and physical properties of cores analyzed in the study.

Core ID	Length (cm)	Classification/ Properties	Collection Location/ Depositional Environment	Clay (%)	Silt (%)	Sand (%)
BH18-211	23	Ice-rich silt	Alaska HWY, Yukon, Canada	11	66	23
BH12F-138	16	ice-rich silty peat (top) and ice-poor silt (bottom)	Alaska HWY, Yukon, Canada	top 8 bottom 12	top 52 bottom 57	top 40 bottom 31
BS19-3-6	19	Diamicton	Dempster HWY, Yukon, Canada	18	51	31
BH20B-337	20	Ice-poor silt	Alaska HWY, Yukon, Canada	8	67	25
DH13-589	26	Ice-rich homogenous peat.	Dempster HWY, Yukon, Canada	N/A	N/A	N/A

Table 2: Root mean square error results for the comparison between the CT, Cuboid and MSCL VIC, EIC and density results.

460

Core ID	RMSE Density CT vs Cuboid (g/cm^3)	RMSE VIC CT vs Cuboid (%)	RMSE VEIC CT vs Cuboid (%)	RMSE Density CT vs Geotek (g/cm^3)	RMSE VIC CT vs Geotek (%)
BS19-3-6	0.14	3	8	0.14	4
BH18-211	0.12	7	9	0.05	8
DH13-589	0.05	1	4	0.03	4
BH12F-138 (top)	0.07	3	7	0.02	11
BH12F-138 (bottom)	0.19	3	2	0.10	10
BH12F-138 (whole core)	0.13	3	5	0.06	10
BH20B-337	0.14	3	5	0.14	3
Overall average	0.12	3	6	0.08	7
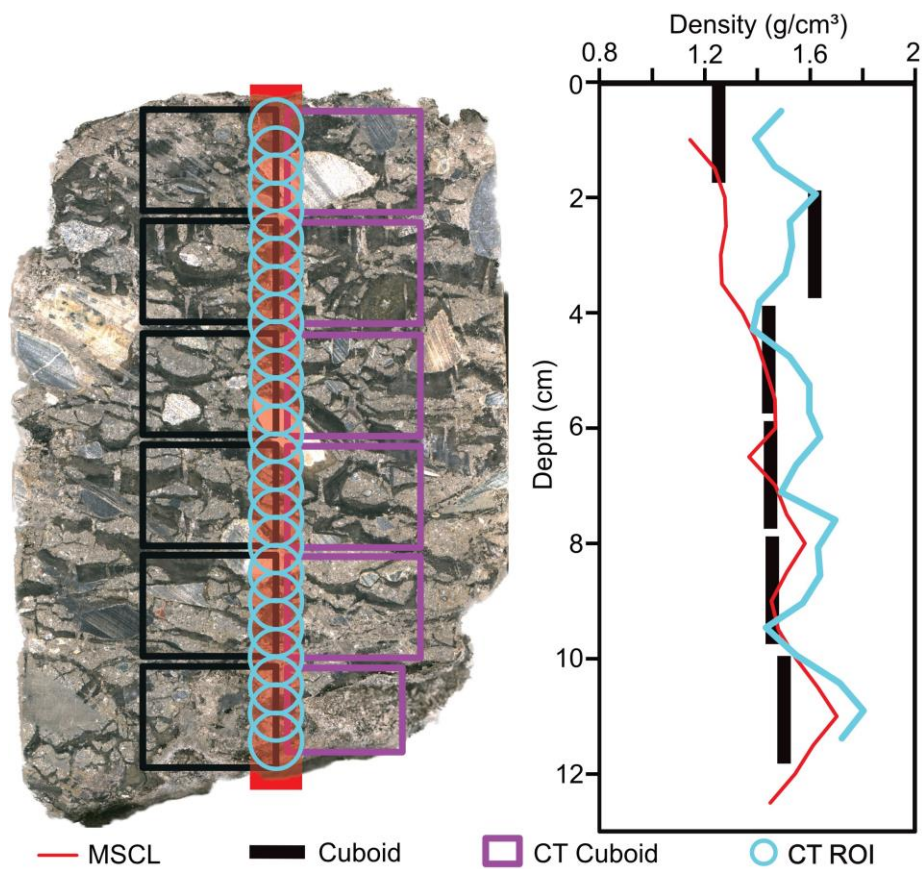
Figure 1: Image of a core highlighting the destructive subsample locations relative to the non-destructive data collection transects.

465
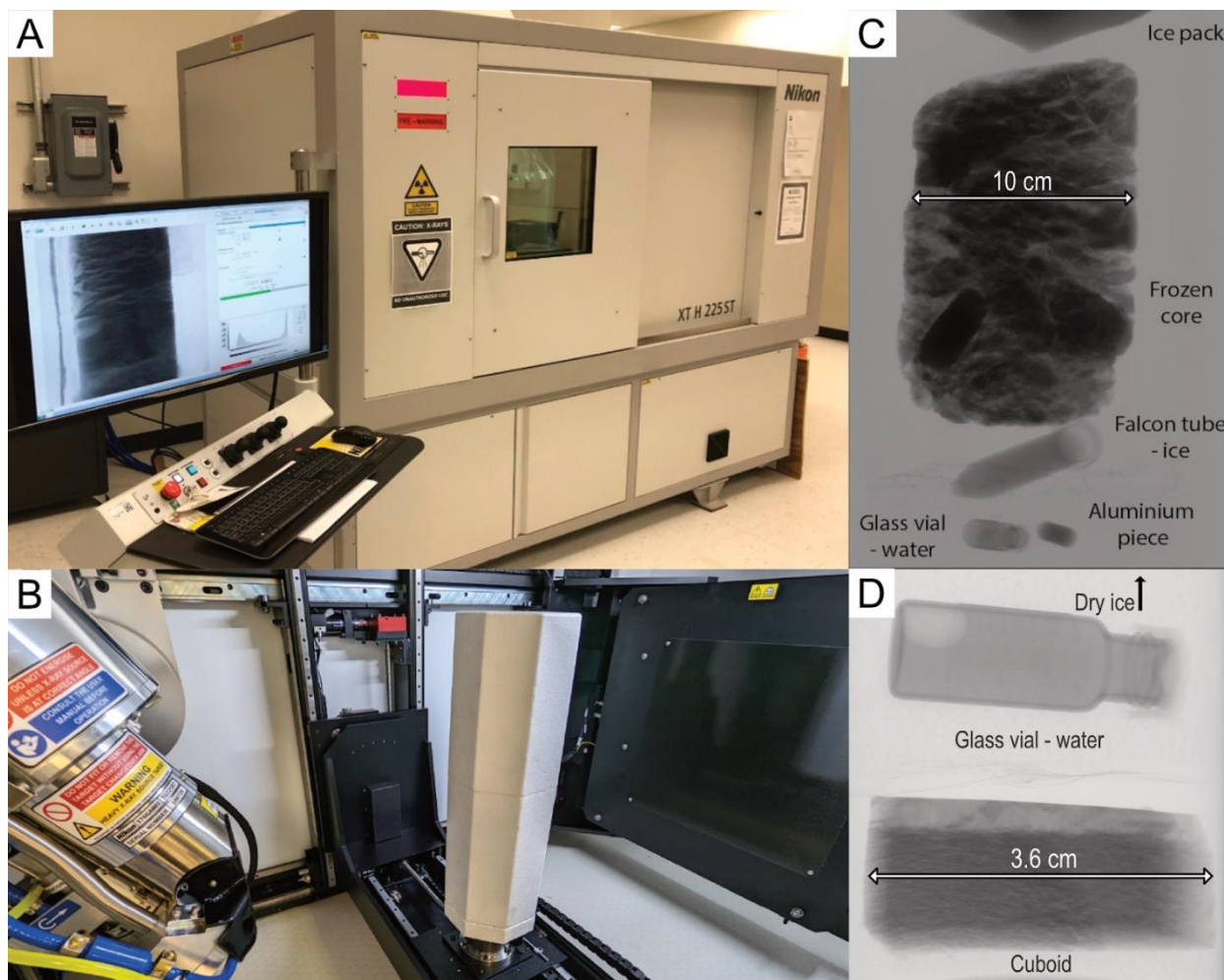
Figure 2: (A) The CT scanner of the PACS Lab.(B) The internal setup for the core scan. (C) X-ray image of the internal setup of the core (D) X-ray image of the internal setup of the cube.

470
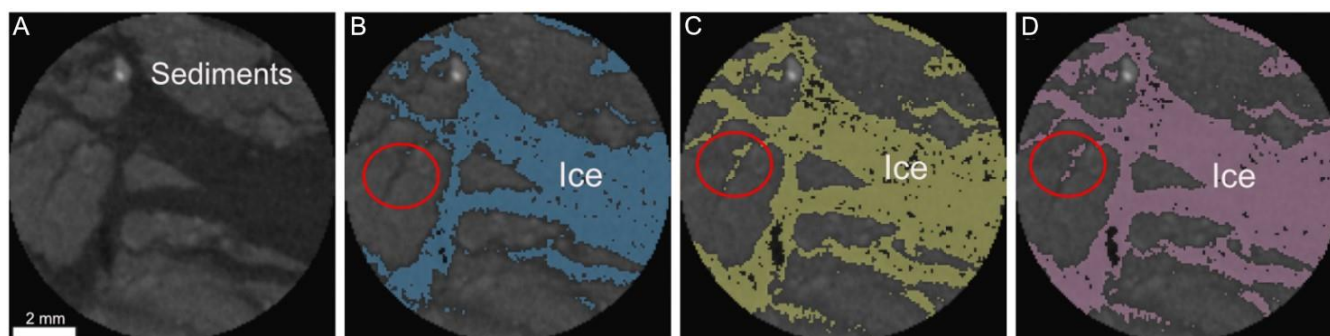
Figure 3: Overview of a slice from ice rich silt core (A) before image processing (B) after the first step, (C) after the second step, and (D) after the third step of image processing using the Otsu method.
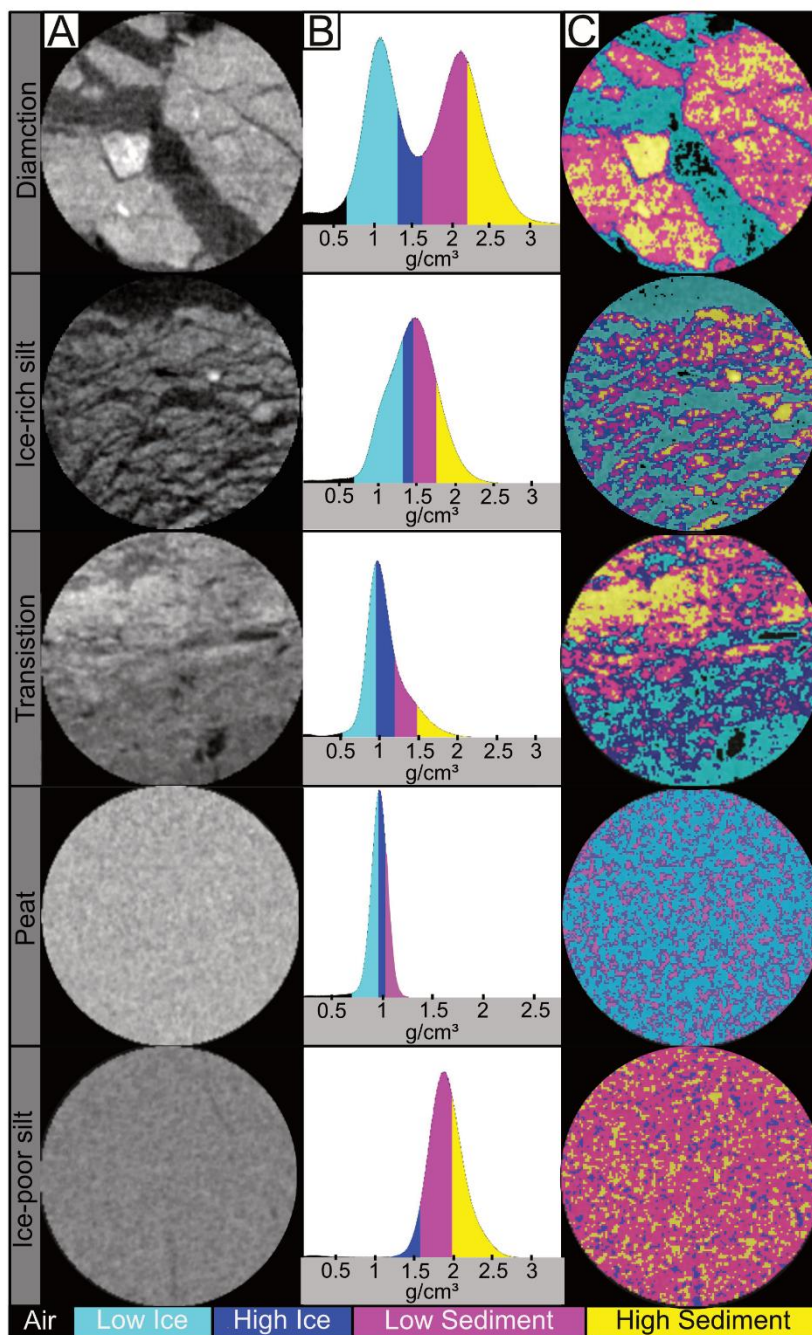
Figure 4: (A) overview of slices from the permafrost cores before image processing **(B)** histograms, and **(C)** image segmentation results
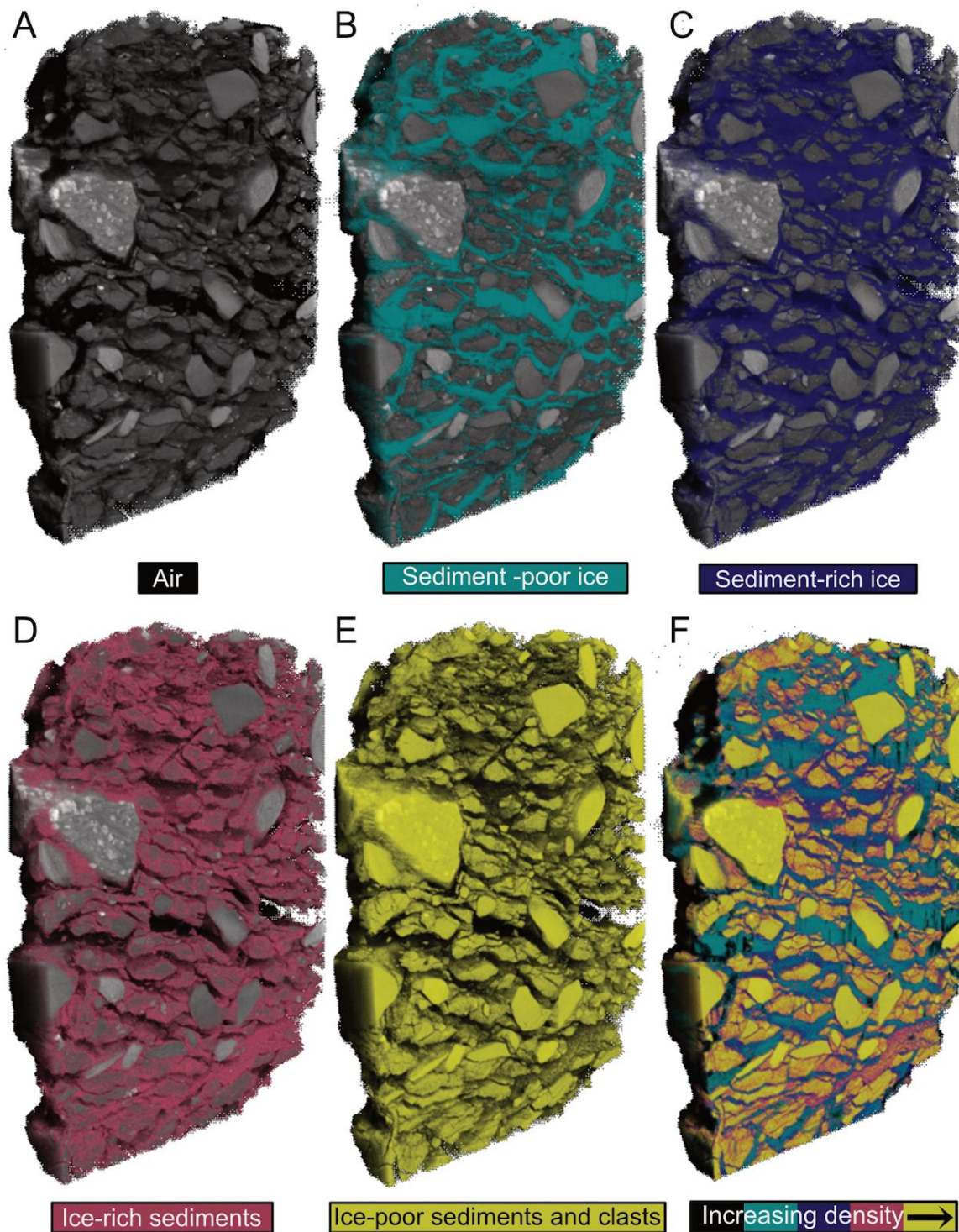
Figure 5: Image segmentation results of the diamicton core

480
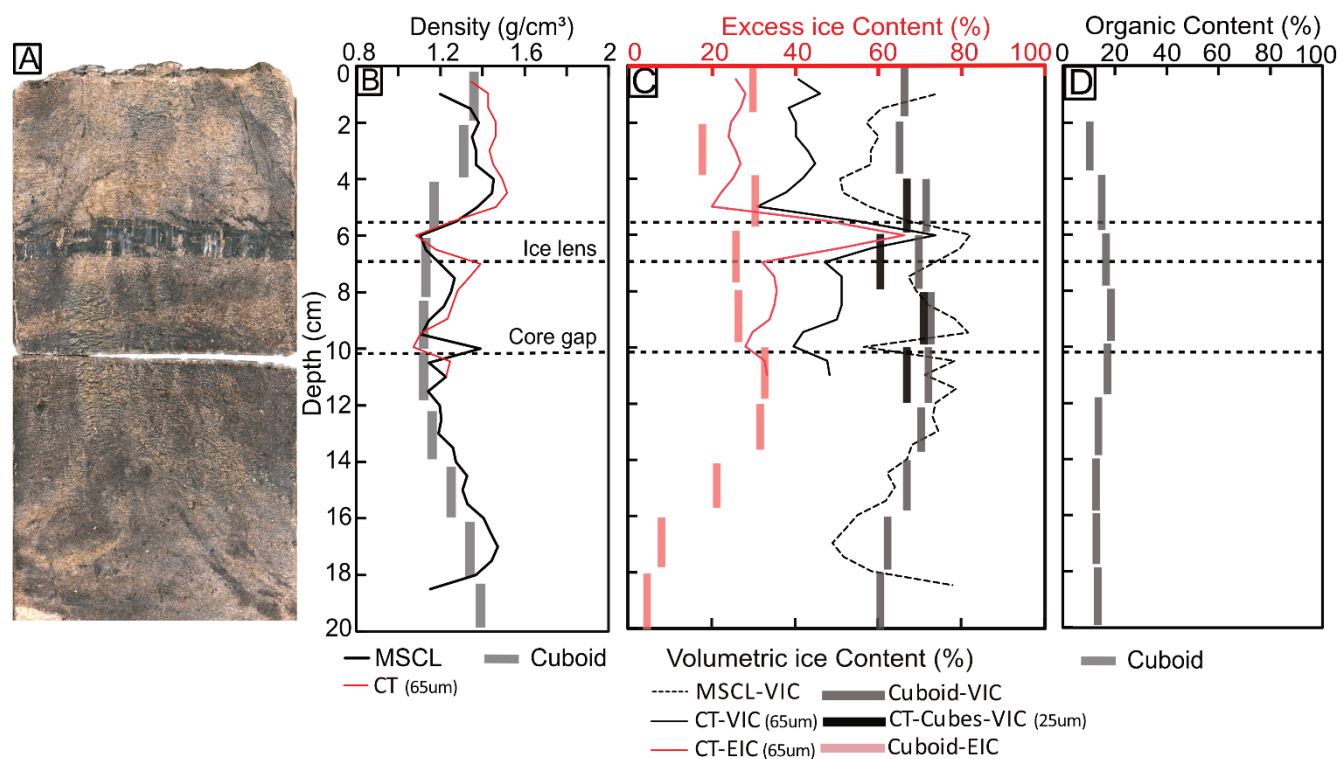
Figure 6: (A) MSCL image of the ice-rich, organic-rich silt core; (B) bulk density; (C) ice contents; (D) organic content distribution in core depth; (E) black and white image of MSCL image with ice highlighted in black.
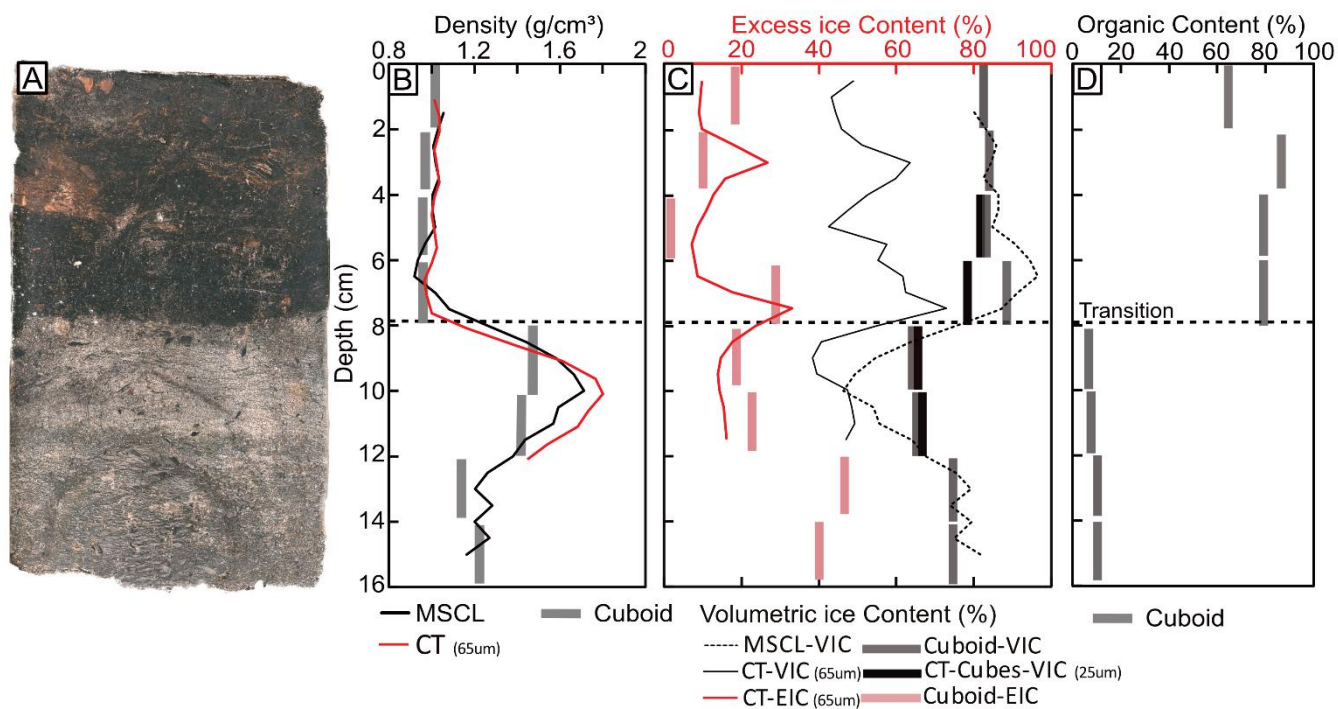
Figure 7: (A) MSCL image of the transition core; **(B)** bulk density; **(C)** ice contents; **(D)** organic content distribution in core depth; **(E)** black and white image of MSCL image with ice highlighted in black.
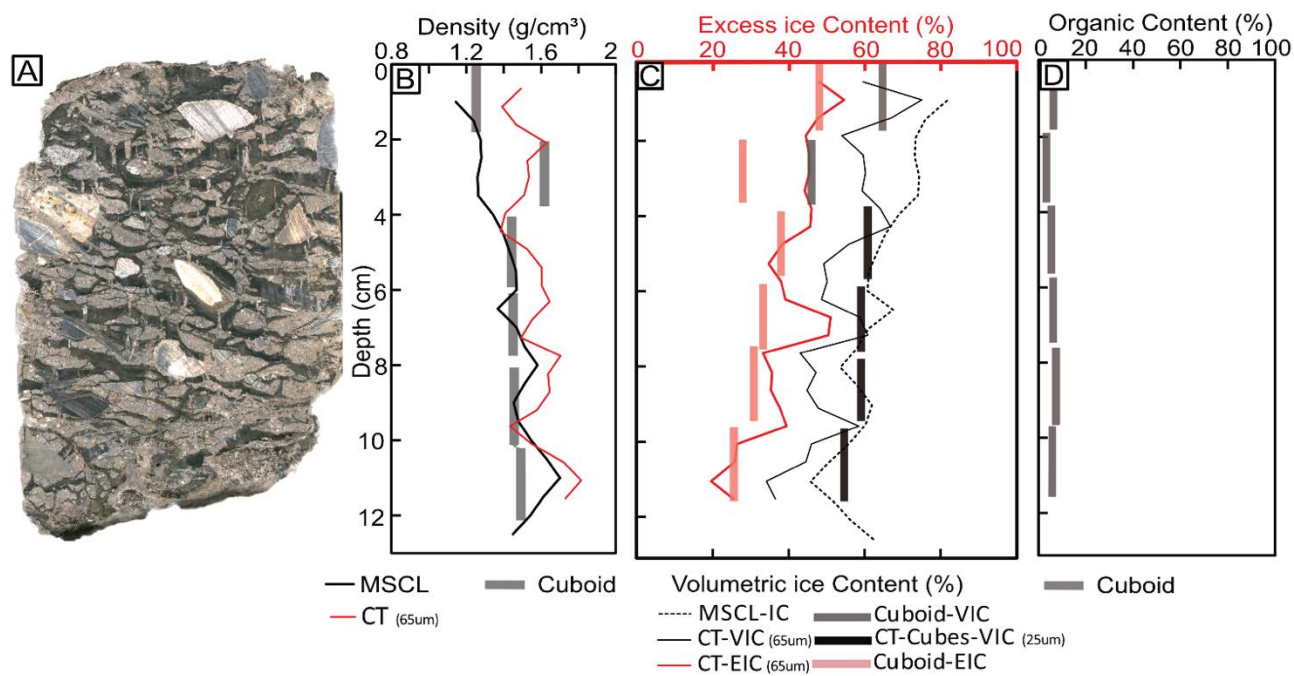
Figure 8: (A) MSCL image of the diamicton core; **(B)** bulk density; **(C)** ice contents; **(D)** organic content distribution in core depth; **(E)** black and white image of MSCL image with ice highlighted in black.
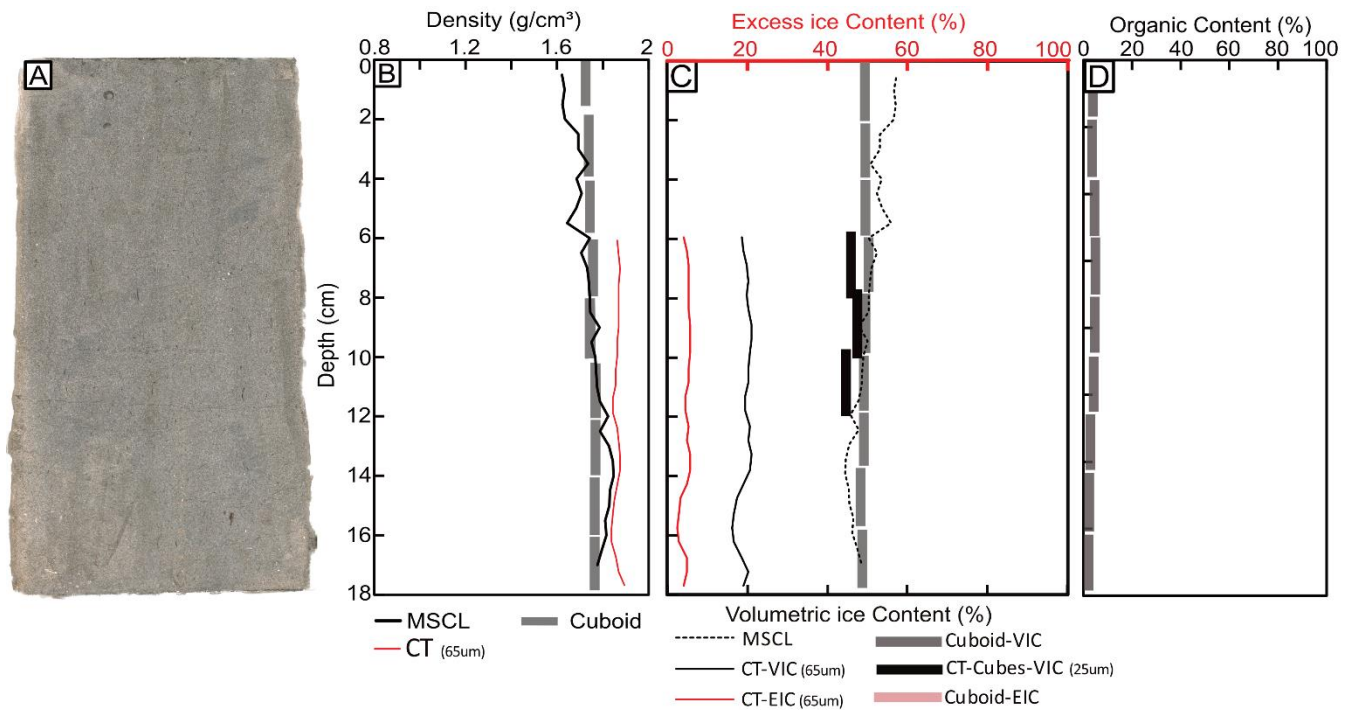
Figure 9: (A) MSCL image of the ice-poor silt core; (B) bulk density; (C) ice contents; (D) organic content distribution in core depth; (E) black and white image of MSCL image with ice highlighted in black.
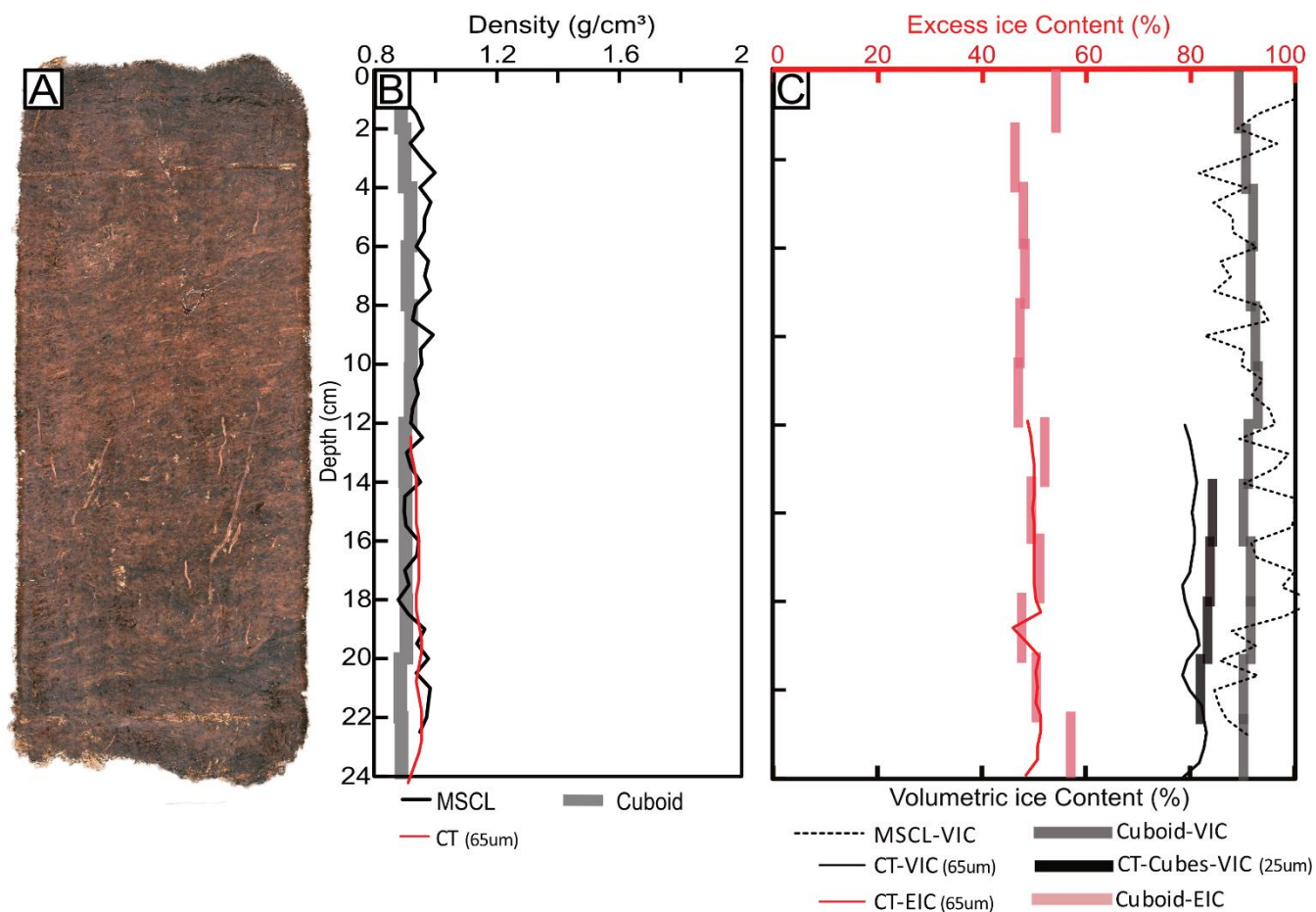
Figure 10: (A) MSCL image of the peat core; (B) bulk density; (C) ice contents; (D) organic content distribution in core depth; (E) black and white image of MSCL image with ice highlighted in black.
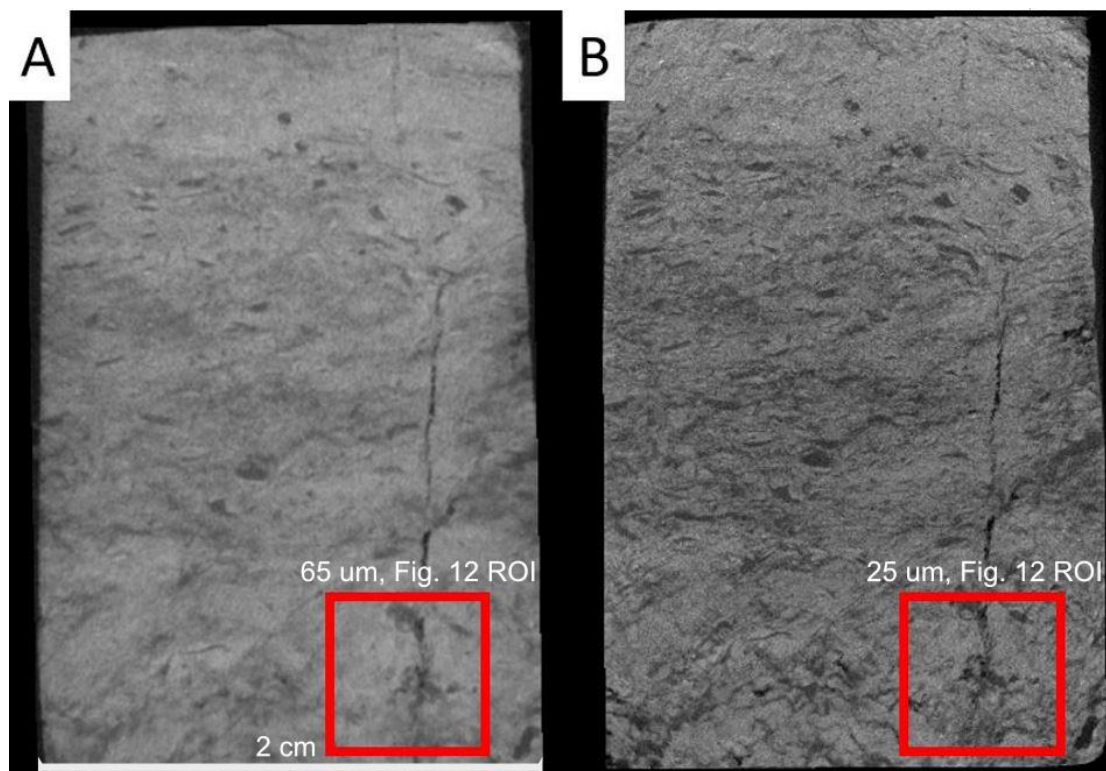
500   **Figure 11: CT images of a cube (BH12F-138-10-12 cm) from the transition core at 65 um (A) and 25 um (B).**
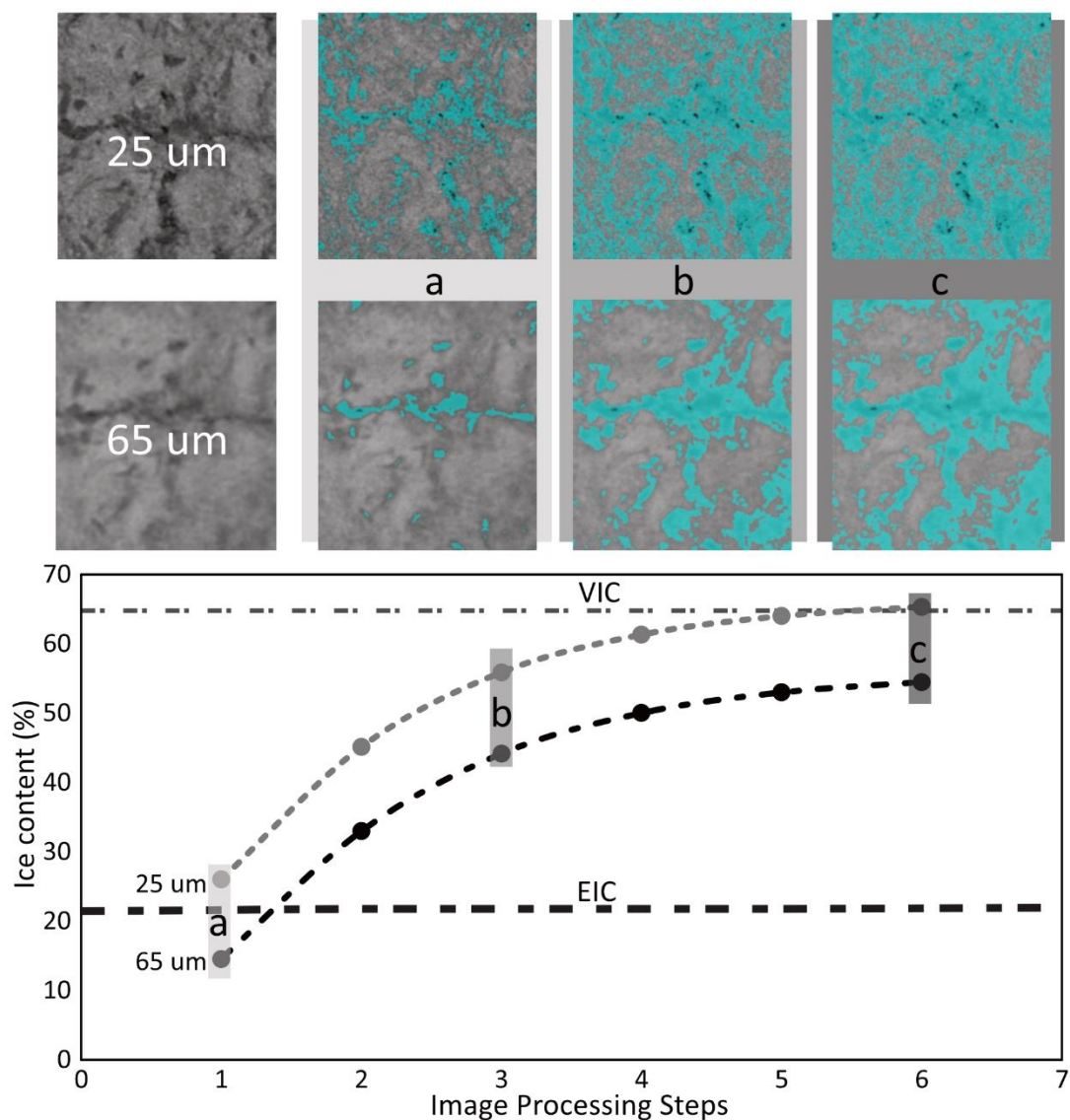
Figure 12: (A) CT ROI's taken from the 65 um and 25 um cube scans (BH12F-138-10-12 cm), (B) Identified ice contents at each image processing step using the Otsu split method.
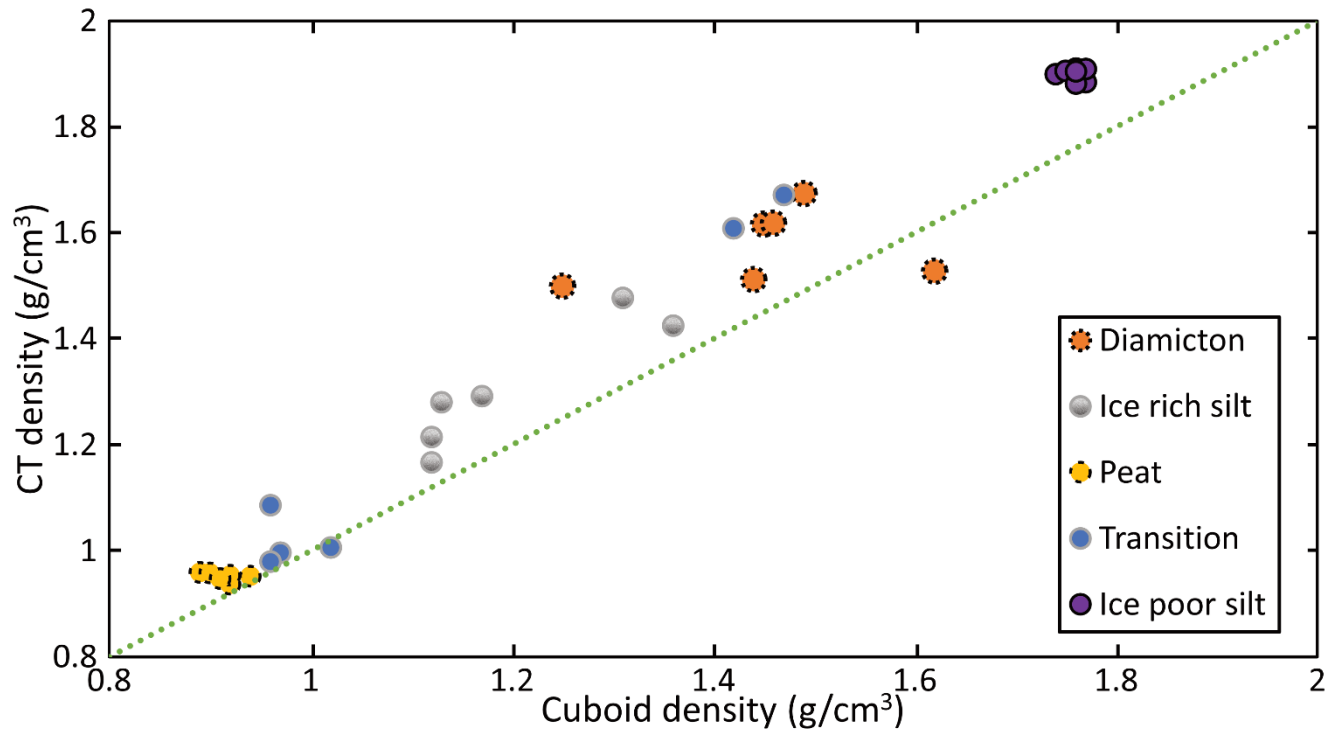
505   **Figure 13: Estimated densities from CT image processing vs calculated ones from cuboid method.**
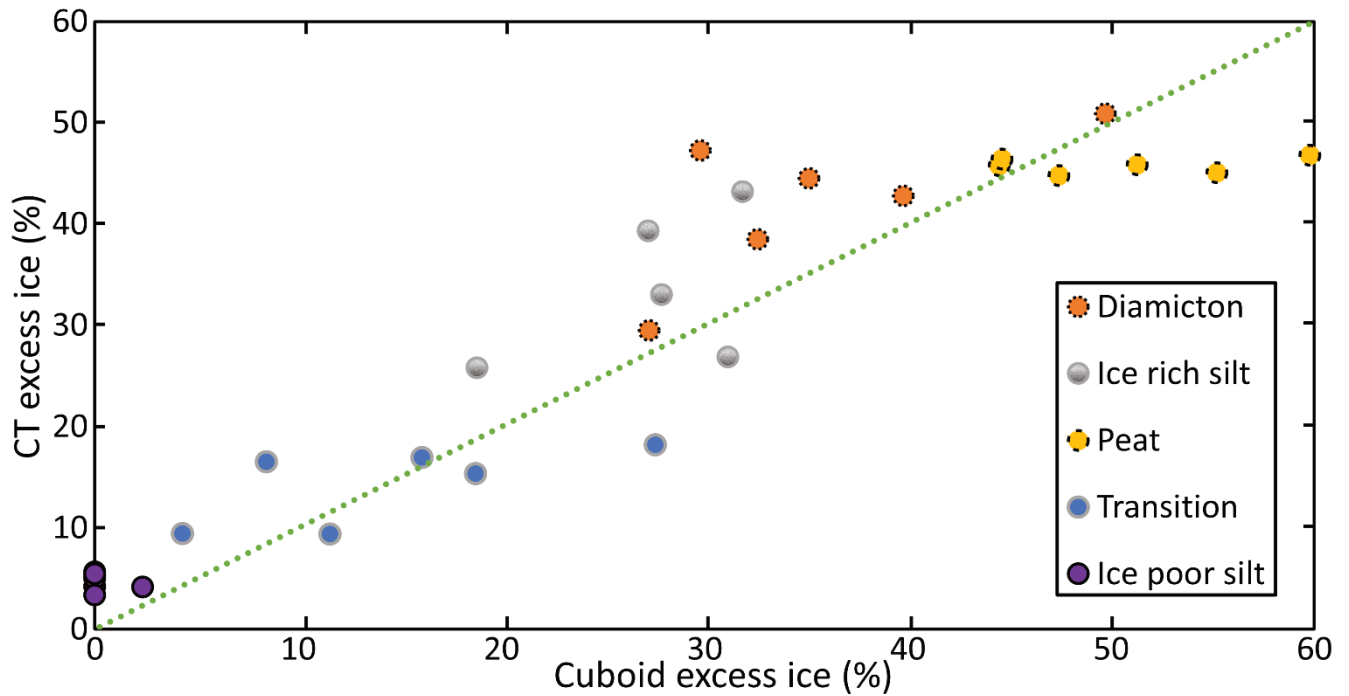
Figure 14: Estimated excess ice contents from CT image processing vs calculated values from cuboid method.
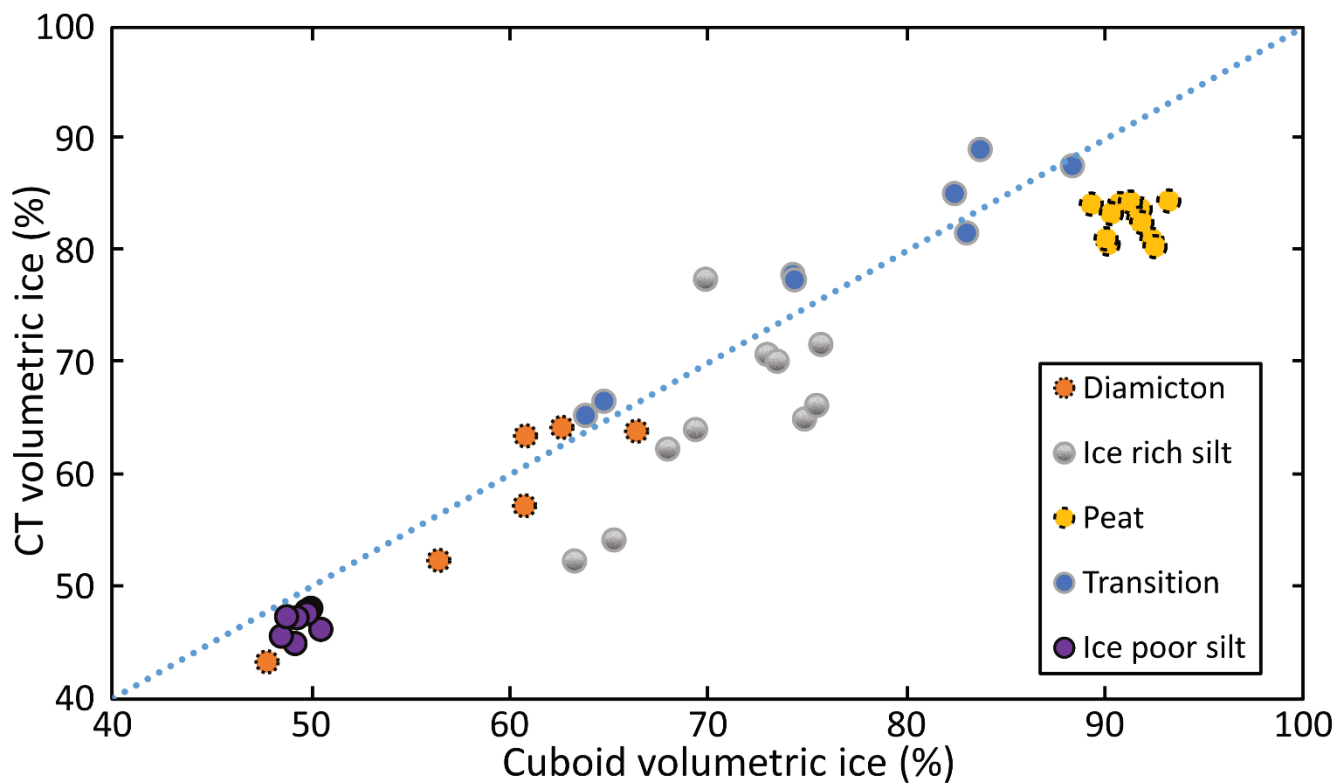
510

Figure 15: Estimated volumetric ice contents from CT image processing vs calculated values from cuboid method.
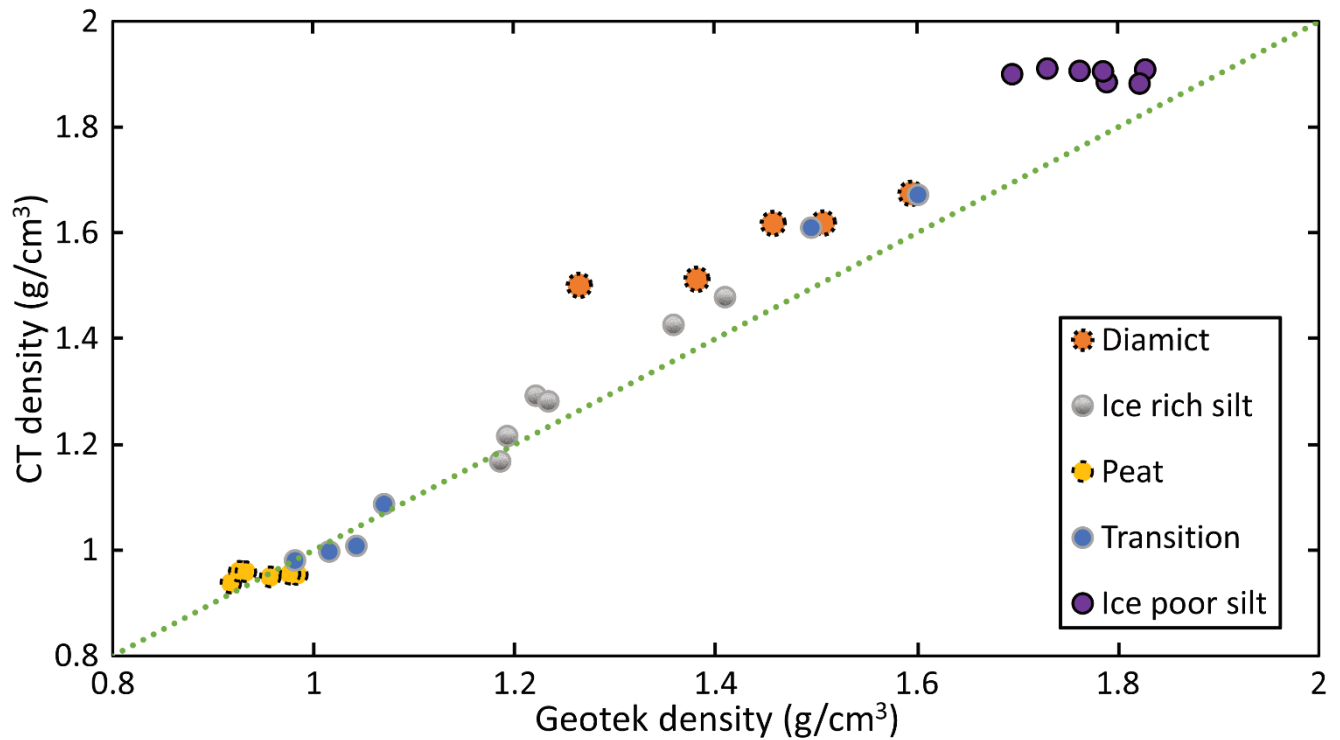
Figure 16: Estimated bulk density from CT image processing vs calculated values from MSCL method.
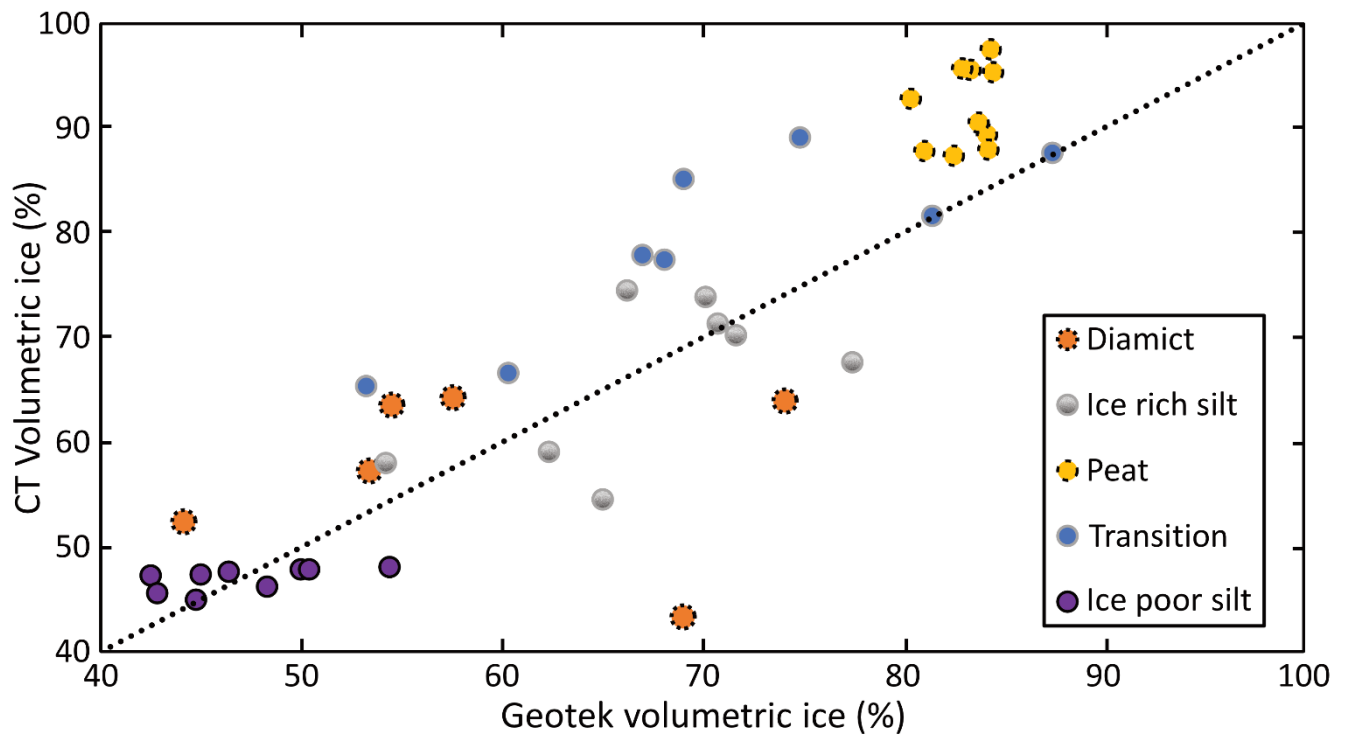
Figure 17: Estimated volumetric ice contents from CT image processing vs calculated values from MSCL method.